M.S. THESIS

Multi-wavelength MEMS Optrode Array for *in vivo* Optogenetics

생체 내 광유전학을 위한 다 파장

MEMS 광탐침 어레이 개발에 대한 연구

BY

SAEYEONG JEON

FEBRUARY 2019

DEPARTMENT OF ELECTRICAL

AND COMPUTER ENGINEERING

COLLEGE OF ENGINEERING

SEOUL NATIONAL UNIVERSITY

생체 내 광유전학을 위한
다 파장 MEMS 광탐침 어레이
개발에 대한 연구

지도 교수 김 용 권

이 논문을 공학석사 학위논문으로 제출함
2019 년 2 월

서울대학교 대학원
전기 정보 공학부
전 새 영

전새영의 공학석사 학위논문을 인준함
2019 년 2 월

위 원 장 _____ **(인)**

부위원장 _____ **(인)**

위 원 _____ **(인)**

Abstract

Saeyeong Jeon

Department of Electrical and Computer Engineering

The Graduate School

Seoul National University

In this research, a new type of multi-wavelength LED (Light Emitting Diode)-based optical neural implant for optogenetic modulation of genetically targeted cells in the brain has proposed. The device is largely divided into two parts, the reusable part and the disposable part. The reusable part is consisted of control electronics with a conventional multi-wavelength LED. The disposable part is comprised with monolithically fabricated microlens array on a silicon die and a manually assembled optical fiber array. Both parts are covered by 3-D printed housing and can be intentionally separated and assembled by snap fit structure. Measured irradiance is 3.35 mW/mm^2 at dominant wavelength 469 nm and 0.29 mW/mm^2 at a dominant wave length 590 nm respectively, when the applied alternating current is 80 mA. The light induced temperature rising is measured and satisfied with the U.S. FDA and IEC standards in all the tested conditions. Also, at 2 mm distance from the fiber tips, over 90 % of the relative light intensity is maintained. In the *in vivo* animal test, the neural activities of a transgenic mouse, expressing Channelrhodopsin-2,

are measured and increased more than double when the device is illuminating the light to the targeted brain area compared to the activities when the device is turning off. Furthermore, through the behavior test with the mouse, the device proves that it can successfully deliver the light and properly stimulate target area, and also, measured results shows that the delivered light can drive the cortical neurons and effect to percept of the mouse. Consequently, the developed device can be applicable to optogenetics application.

Keywords: Optical neural implant, Multi-wavelength, Optogenetics, Microlens array

Student Number: 2017-26273

Contents

List of Figures

List of Tables

Chapter 1

Introduction

1.1 Background

To understand how neural circuits which are consisted with a plethora of interconnected neurons with various size, formation, activity patterns, and types in each part of the brain act and communicate each other, are one of the most challengeable tasks in the neuroscience fields. Also, studying the working mechanisms and interrelations of neural circuits are critical both for comprehending malfunctions of neural circuits causing neurological disorders such as Parkinson's disease (PD), schizophrenia, and epilepsy and for developing targeted therapeutic strategies for them.

Neural interfaces which are available for interfacing with neural circuits and recording or modulating its activities have been developed for a few decades in neuroscience fields. Neuroscientists are taking advantage of these interfaces for temporally precise manipulation of neuronal activities which can be able to elucidate the casual functions of individual neuron types and for brain mapping . Thus, for expanding knowledge and deeper understanding of the complex brain networks consisted with a myriad of interconnected neurons, it is imperative that a selective activation and inhibition of specific target neurons should be precisely controlled.

In figure 1.1, there are several types of interventions for stimulating neurons such as electrical stimulation of neurons through the application of current (A), stimulation of neurons through the application of a transcranial magnetic field (B), cell type-specific optical stimulation or inhibition of target neurons expressing light sensitive opsin proteins (C) [1]. In case of electrical and magnetic stimulation of neurons, it can activate the neurons with regional targeting capability, but without neuron-type specificity which means unlike optical activation of neurons, in spite of having represented a major breakthrough in the field of neuroscience, those technologies have a critical drawback of poor spatial resolution, and thus stimulate a wide array of cells without selectivity in the neural network surrounded near the target cells and impede the specification of the roles of targeted specific neurons. In 1999, the possibility of using optical stimulation for selectively probing and controlling neural activities with precise methods was suggested by Crick in his lecture [2]. As a result of advances in neuroscience fields through overcoming those limitations, a new field of

study in neuroscience has emerged : optogenetics [3].

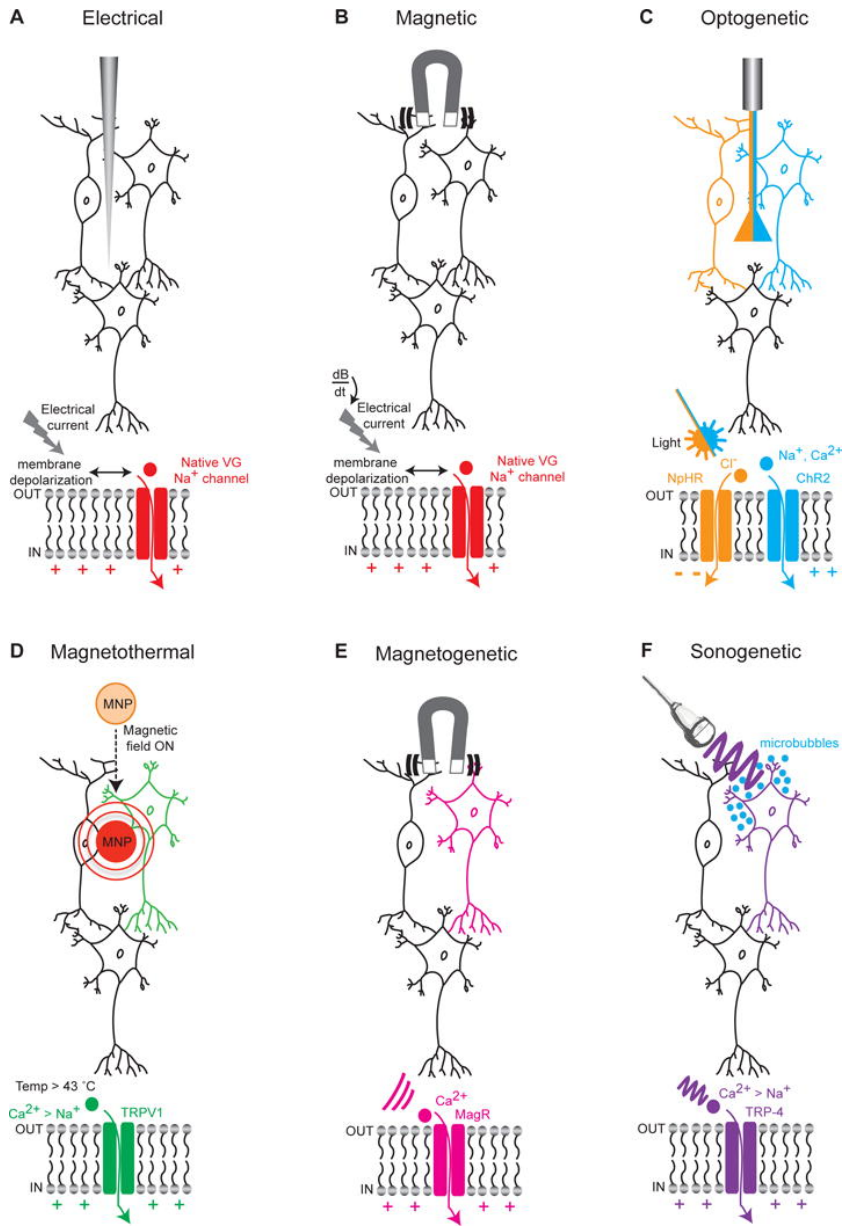

Figure 1.1 Several types of technologies for stimulating neurons [1].

1.1.1 Optogenetics

The compound word “optogenetics" is formed from the words “optics" and “genetics” which combines optical and genetic methods to stimulate or inhibit specific targeted cells of living tissue that are transfected neurons that express opsins on their membrane surface, using optical sources especially visible light. In a broad meaning, optogenetics is a neuromodulation method and a biological technology which can be able to deliver specific light into tissues, target interested cells, typically neurons, obtain signal information such as electrical recordings and targeted imaging from the neurons’ activity pattern, and analyze it [4]. Due to its unique characteristics such as providing millisecond-scale temporal precision, cell-type selectivity which can specifically readout of neural signals, and having high spatiotemporal resolution, as time goes by, its importance in neuroscience fields is getting bigger and bigger.

Since the concept of “optogenetics” was established, many studies have been carried out so far to prove that how specific neurons in the brain contribute to the functions of neural circuits by analysis action potentials and fluctuations in the local field potentials which cannot be identified using conventional electrical stimulation methods. The neuro modulations in the activity of transgenic neurons that express optogenetic actuators, so called opsins, on the surface of neuron’s membrane are induced by optogenetic stimulation of optical implants. The figure 1.2 comprehensively shows the principle for stimulation of neurons in optogenetics. Unlike the conventional electrical stimulation of neurons, the

transgenic neurons having certain types of opsins, which function as channels for transporting specific ions through either depolarizing or hyperpolarizing the cell, are activated by the optical simulation. Using the light delivery, the activation patterns of target transfected neurons are controlled. For instance, Channelrhodopsin (ChR2) is a common opsin that can excite the neurons and depolarize neurons by illumination of blue light (460~470 nm), and Halorhodopsin (NpHR) can inhibit the neuron by hyperpolarizing with yellow light (589 nm), respectively [4]. In table 1.1, there are various types of opsins with its characteristics such as a gate type, activation specific wavelength, the effective power density for 50 % activation (EPD 50).

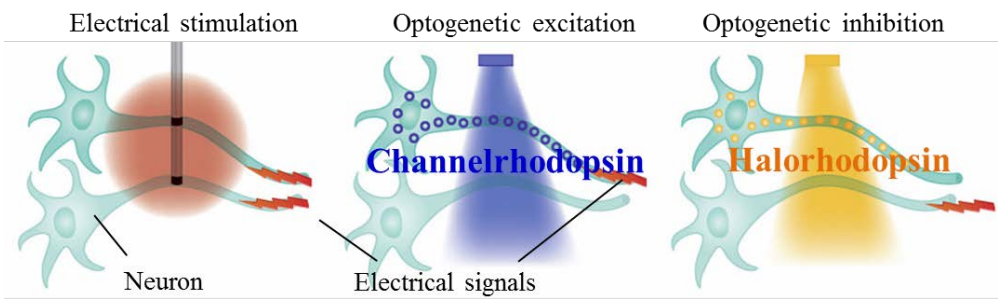

Figure 1.2 Principle for stimulation of neurons in optogenetics [4].

Table 1.1 Characteristics and parameters of various opsins used in optogenetics [5].

Opsin type	**Opsin subfamily**	**Gate type**	**Activation λ (nm)**	**EPD 50 (mW/mm^2)**
Channelrhodopsin	ChR-2	Cation channel	460	1.3
Channelrhodopsin	VChR1	Cation channel	589	~ 0.5
Halorhodopsin	eNpHR3.0	Chloride pump	589	5.4
Archaerhodopsin	Arch	Proton pump	566	~ 7.5

Note: EPD50, effective power density for 50 % activation.

1.2 Previous study

In 2007, the first demonstration of *in vivo* control of mammal's motor cortex has been conducted by a team of Deisseroth at Stanford University. The optical interface was consisted with a blue solid-state laser (473 nm) and multimode optical fiber [6]. Since then, a myriad of optical interfaces have been developed and tested for a field of optogenetics. In figure 1.3, there are various types of optogenetic probe designs such as a multi electrode array with a single optical waveguide, a silicon neural probe with monolithically integrated optical waveguide, and a neural probe consisting of a microfluidic channel and electrodes, surrounded by waveguides [7]. Until now, The development of optical interfaces has evolved in two major directions: laser-coupled optical neural implants and LED (Light-Emitting Diode)-based optical neural implants, both having different light sources.

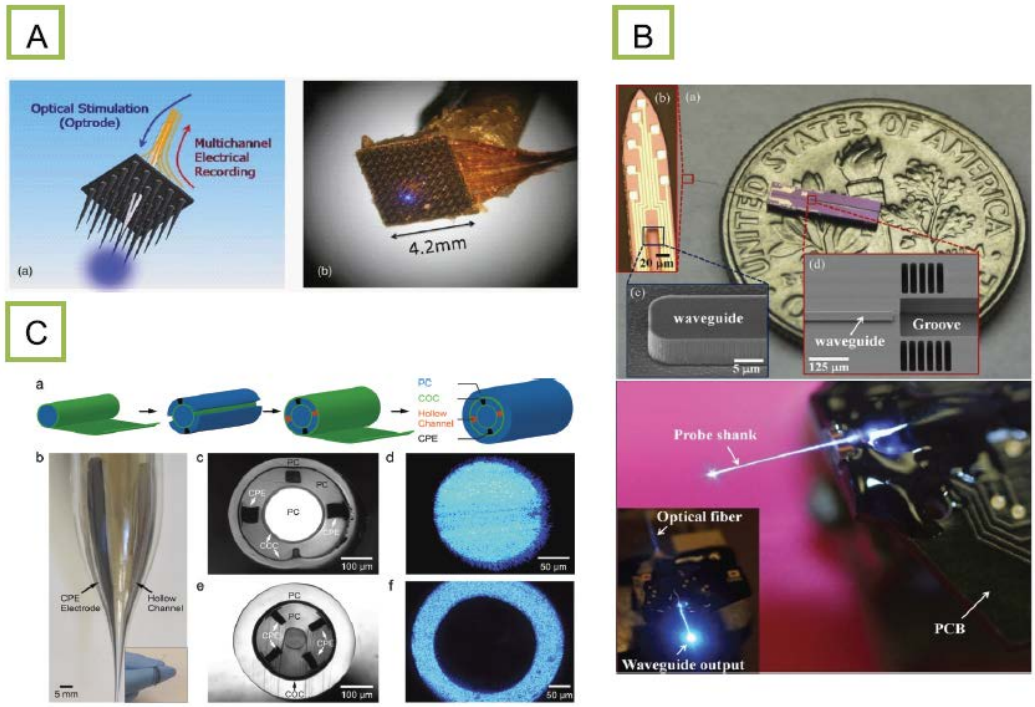

Figure 1.3 Comparison of various fiber/waveguide optogenetic probe designs [7].

1.2.1 Laser-coupled optical neural implants

Due to the minimum irradiance for neural stimulation of certain opsins such as Channelrhodopsin (ChR2), and Halorhodopsin (NpHR), the high light power systems have been widely used for various optogenetic fields. One of the systems is laser based optical neural interfaces which use laser light source and optical light delivery system such as optical fibers, monolithically integrated micro-waveguides, and tapered waveguides with electrodes. Figure 1.4 shows several typical types of laser based optical interfaces [8]. (a) is a optrode system with one multimode optical fiber and hollow core filled with 50 μm

thick recording wire [9], (b) is a different optrode system with a 200 μm thick multimode optical fiber and integrated four tetrode bundles [10], (c) is a Utah multielectrode array with a multimode optical fiber which is replaced with one recording probe [11], (d) is a Michigan silicon neural probe with monolithically fabricated optical waveguides and microfluidic channels [12], and (e) is a bundle of in-plane neural probes with waveguide combs which is fixed on the baseplate holder [13]. All of those kind of laser based optical neural probes have tethered systems which can deliver the light from the outside of laser light source using optical waveguide especially optical fibers, and thus within the limitations of operating of laser source, the tethered systems are adjustable in the long range of electrical demands of the light source and can deliver much higher light power. Furthermore, the laser based optical implants have several unique advantages such as high light coupling efficiency, low beam divergence over a long distance from s outside light source to target cells, and narrow spectral bandwidth.

Despite the laser based systems' unique characteristics, the nature of a tethering system which the optical fiber cord detached to the animal's target area is connected with a external laser light source to selectively deliver light, could be high possible impediments for behavior experiments of freely moving animal such as tangling between the optical fiber cord and the animal, causing unintentional rotational force between inserted device and surrounded tissues, and reducing the reproducibility of *in vivo* tests. Moreover, due to the unique configuration of butted fiber optic interconnection, the illumination of a broad neural region and the use of light with different wavelengths for excitation and inhibition

in the same region are very challenging tasks for conventional laser-based systems. A costly laser system, high power consumption, unstable illumination, and long warming-up time are additional obstacles of laser based optical neural implants.

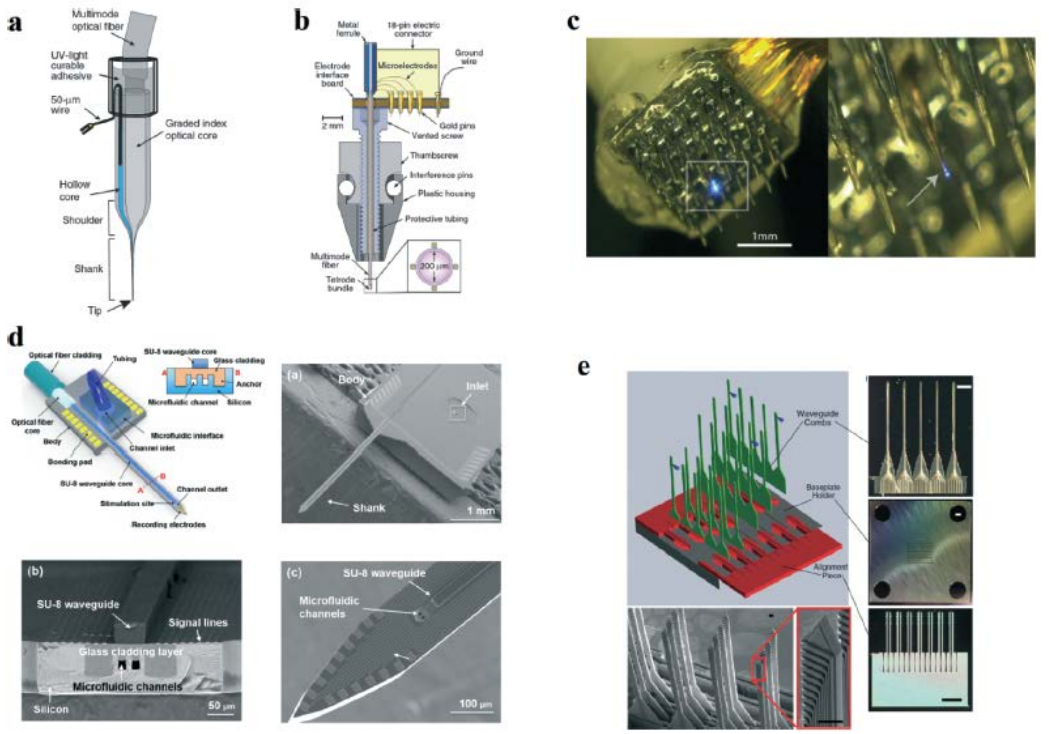

Figure 1.4 Examples of laser-based optical neural implants [8].

1.2.2 LED-based optical neural implants

LED-based optical neural implants have been widely used as counterparts of the laser system due to its unique advantages. Unlike the former laser-based optogenetic devices,

the LED-based optogenetic devices can stably illuminate the target cells within intentionally selected wavelengths, have considerably lower power consumption compared to the laser system, and be readily available for switching wavelength when the device is operating without additional devices. Most of all, since the LED-based optogenetic device is specifically suitable for a fully wireless system to enable a freely behaving animal's *in vivo* experiments, various types of LED based neural implants have been developed.

Due to the development of MEMS technology, not only the device using optical fibers as a light delivery system has been used, but also, silicon-based neural probes have been developed. Typical examples of silicon-based implants are Michigan probe and Utah probe. In case of Michigan type neural probes, the designs are widely accepted because of several favorable characteristics for neurological experiments such as precisely controlling of probe dimension, very compact and small size to reduce device invasiveness and inevitable neural damage, multiple recording sites along the length of a shank, and enhancing biocompatibility. Although those neural probes can provide both a compact design and decreasing neural damages, it still has a high possibility of crack and shatter and problems of neural damage due to high Young's modulus mismatch with surrounded tissues and surface of neural probe.

The monolithically fabricated μLED-coupled optical neural implants has developed. In figure 1.5, there are typical type of μLED based optogenetic devices [8]. (a) is a sapphire substrate based high density μLED array fabricated by microfabrication technology [14], (b) is a Opto-μECoG array on flexible Parylene-C substrate with ITO electrodes [15], (c)

is a μLED-coupled optical fiber array fixed on the silicon die with electrode line [16], (d) is a μLED-coupled SU-8 micro-waveguide array with multilayer of ITO, Parylene, gold, and Parylene [17], (e) is a μLED neural probe fabricated from an epitaxial GaN/sapphire substrate using MEMS technology [18], and (f) is a polymer based flexible multichannel neural probe with temperature sensor, neural recording microelectrodes, light intensity sensor, and μLED [19]. Even though μLED mounted on a neural interfaces can provide high spatial resolution, low power consumption, and high light power, several challenges still remain such as localized heating due to direct contact with surrounded tissues, light-induced artifacts, and extremely complex fabrication of device. The temperature rise of the operating neural implants should be lower than 0.5 to 1 °C [20].

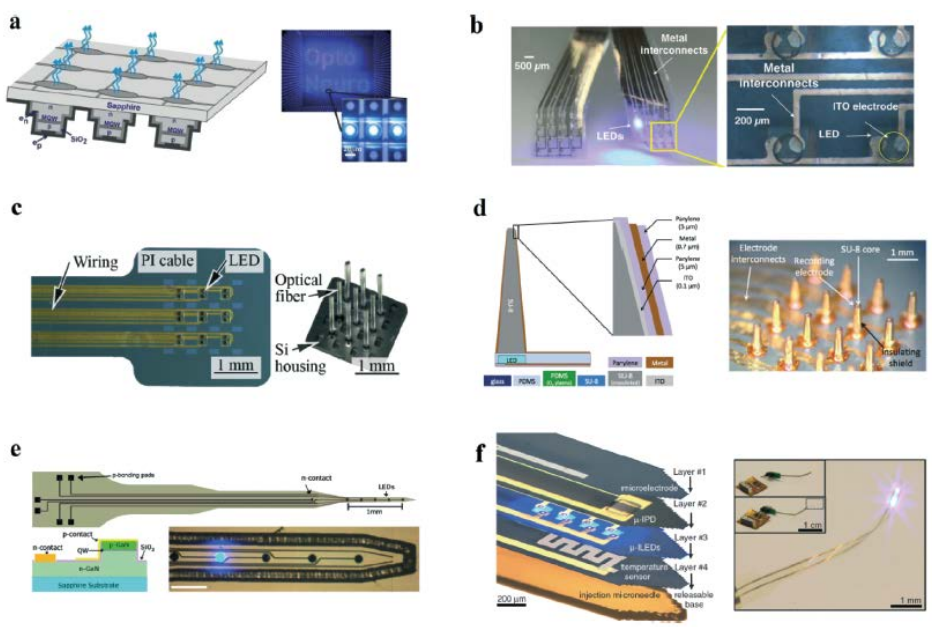

Figure 1.5 Examples of μLED-based neural interfaces [8].

1.3 Purpose of the research

In this research, a new type of multi-wavelength LED-based optical neural implant for excitation and inhibition of target cells is presented. The developed device ultimately will be adapted to fully wireless systems for optogenetics. The purpose of this research is that verify the feasibility of the multi-wavelength illumination system by using a single conventional LED, scalability of the aligned optical fibers, and ability to stimulate of multiple target area. First of all, obtain optimized design layout through previous research. The device is consisted with both disposable and reusable part which can make easily separate and combine to facilitate biochemical experiments. The square-shaped glass microlenses with a highest fill-factor are connected with 4x4 optical fibers with a high numerical aperture (NA=0.5) for high coupling efficiency, and the device is installed under the bottom of disposable part. Due to the array configuration of the light delivery system, multisite of the target area can be stimulated at the same time. The reusable part is consisted with a control electronics, and a conventional multi-wavelength LED as a light source which can be able to reduce the complexity of the system, operating power consumption, and total system cost. By physically separating the LED light source from the part that is stimulated by delivered light, the possibility of temperature rising caused brain damage is minimized. Next, fabricate the fully assembled device with suitable 3D printed housing for *in vivo* animal experiment. Lastly, verify the feasibility of the fabricated device for optogenetics application by several experiments.

1.4 Layout of the paper

In chapter 2, the overall design for the suggested multi-wavelength LED based optical neural probe is introduced, which includes the details of each part of the device with specifying of dimensions and components. Chapter 3 describes the fabrication process of the device, assembly, and fabrication results in details. In chapter 4, to verify the feasibility of the developed device for the optogenetics, optical and thermal characteristics are measured and analyzed, also through the *in vivo* animal test with the developed device, the actual applicability for optogenetic research is confirmed. Finally, chapter 5 deals with the conclusion of this research.

Chapter 2

Design

2.1 Overall design

Figure 2.1 shows the overall design of the proposed multiwavelength LED-based optical neural probe in cross-sectional view. The implantable optical neural probe is divided into two parts. The disposable part is composed of 4x4 square-shaped borosilicate glass (BSG) microlens array (MLA) connected with a 4x4 array of high NA optical fibers (FP200URT, Thorlabs, Inc.). The reusable illumination part consists of control electronics with a single packaged multi-wavelength LED and a resistor mounted on a PCB (Printed Circuit Board) and external power supply lines. 3-D (3-dimensional)-printed acrylonitrile butadiene-styrene resin (ABS-LIKE, CUBICON, Inc.) has been used for upper and lower housing

parts, which have a latch structure for simple snap-in assembly and separation. Optical fibers are inserted into the target region of the brain, and the disposable part is attached to the skull with dental cement during the animal experiment.

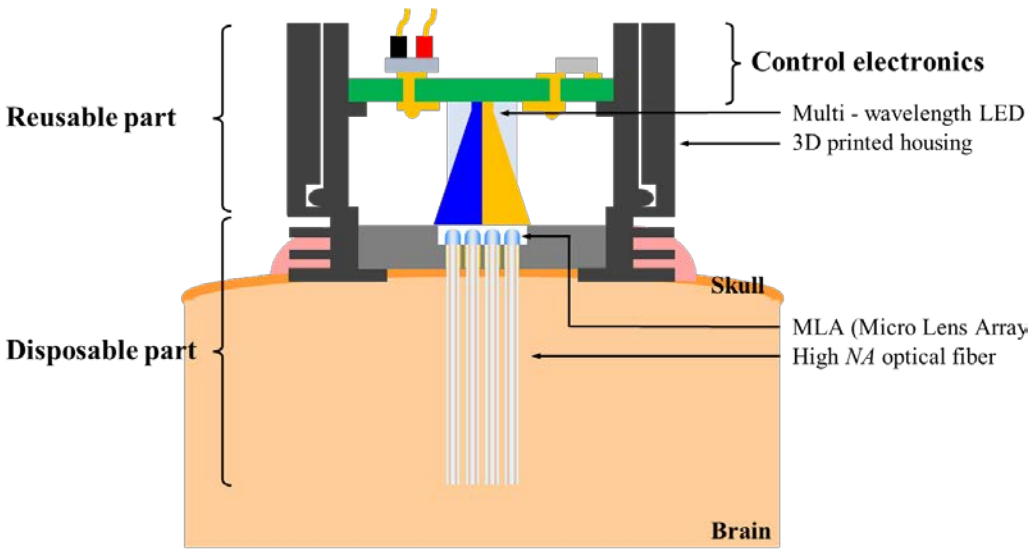

Figure 2.1 Cross-sectional view of the multi-wavelength LED based optical neural implant.

2.1.1 Microlens array

The square-shaped glass microlenses has been designed for the highest possible fill-factor and fabricated by glass reflow processes. Each microlens has an area of 300x300 μm^2 and a core-to-core spacing of 320 μm (Figure 2.2 left). On the bottom of the silicon die, there are 4x4 alignment holes which have a diameter of 250 μm (Figure 2.2 right). This array configuration of light delivery system are applicable for multi illumination in a wide range

of brain to stimulate simultaneously after assembling with multimode optical fibers that have a high numerical aperture (NA=0.5) for high coupling efficiency.

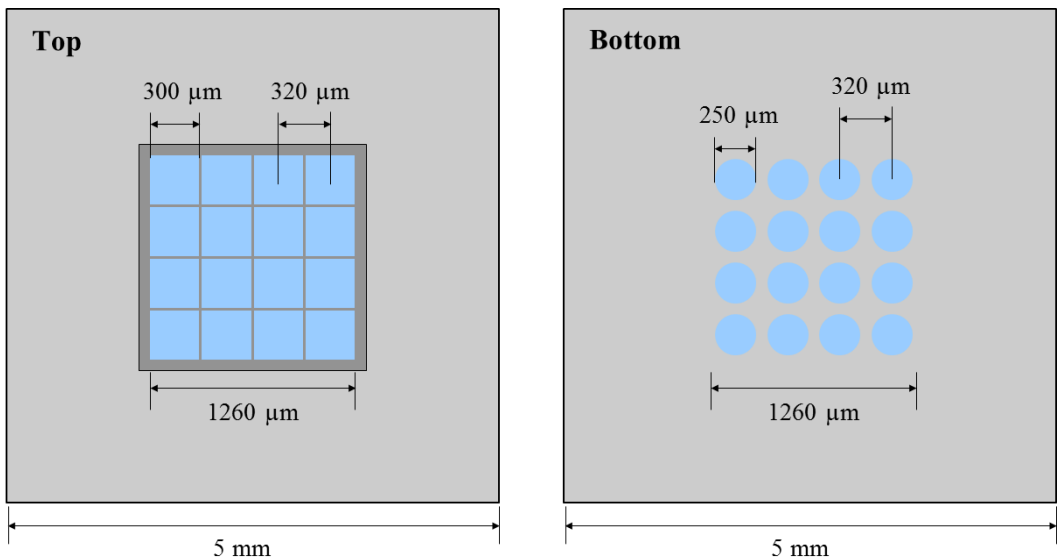

Figure 2.2 Top and bottom view of the glass microlens array on the 5 x 5 mm^2 silicon die with specific dimensions.

2.1.2 Control electronics

The control electronics has been consisted with a conventional domed type multi-wavelength LED (N500TBY4D, LigCom LED Group), a 22 Ω SMD type resistor, and a power source on a PCB (Printed Circuit Board) which has an area of 10x10 mm^2, the thickness of 1.6 T, and two layers (Figure 2.3). Due to the using of a conventional type of LED for a light source of this device, it would significantly reduce the system complexity,

power consumption, and system costs. The input power of this device is depended on a LED and it should be operated under the recommended conditions that the maximum DC forward current is 30 mA, the peak pulse forward current is 100 mA each, and the average forward current is 30 mA at operating temperature between - 40 and + 85 ℃.

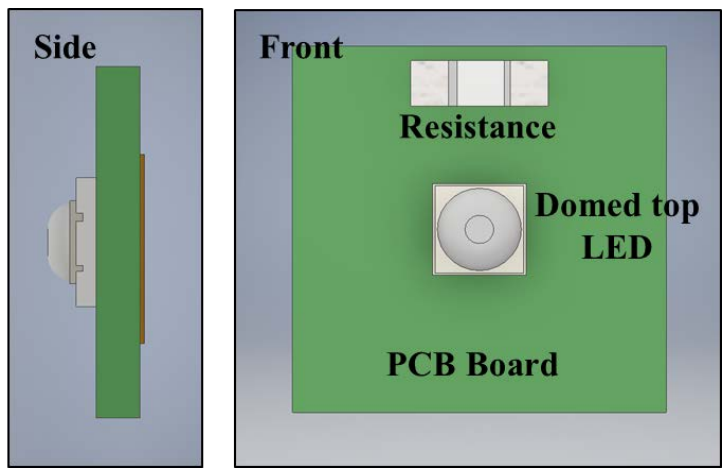

Figure 2.3 Side and front view of the control electronics with multi-wavelength domed top LED.

2.1.3 Housing

The housing parts have been consisted with large two parts which are top and bottom parts for disposable configuration. The reusable part which is a top part has designed for control electronics having a single conventional multi-wavelength LED as a light source. Also, at the end of the part, there are four rounded latch structures for putting it in and out easily,

which is suitable for disposable configuration. The upper part has a volume of 10 x 10 x 10 mm^3 which can be assembled with a bottom part (Figure 2.4, Top part).

The fabricated silicon die will be installed in the bottom part with adhesive and fixed on the skull part of the brain with the cement. The wing-like layered structure at the low of the bottom part allows the device to be more easily secured to the skull. The bottom part has a volume of 64π x 10 mm^3 which can be assembled with a top part of housing (Figure 2.4, Bottom part).

All the designed top and bottom parts will be made using 3-D (3-Dimensional) printer with acrylonitrile-butadiene-styrene resin (ABS-LIKE, CUBICON, Inc.).

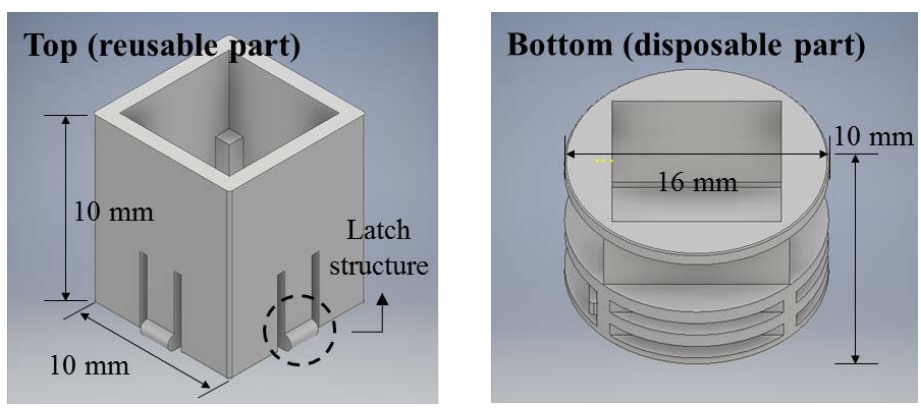

Figure 2.4 Top (reusable part) and bottom (disposable) view of the design of housing parts.

Chapter 3

Fabrication

3.1 Fabrication of microlens array

3.1.1 Fabrication processes

The glass microlens array has been fabricated with MEMS (Micro-Electro Mechanical Systems) technology (Figure 3.1). First of all, the DRIE (Deep Reactive Ion Etching) has been proceeded for making cavities on the 1 mm-thick silicon wafer. The cavities have been filled with plasma treated BSG by anodic bonding and annealing process. After planarization of surplus glass by CMP (Chemical Mechanical Polishing) process, the height of a glass column has been controlled through the dipping in HF (Hydrofluoric Acid)

solution. The time management is the key factor of producing targeted height of glass columns. The second DRIE has been carried out to form square pillars and after a second thermal reflow process, the square-shape glass MLA has been formed on the silicon wafer. The backside DRIE has been proceeded for a formation of guide paths of optical fibers with alignment of each center of glass MLA. Finally, the silicon die has been diced into 5 mm x 5 mm with a dicing saw machine.

(a) Surface plasma treatment on BSG

(b) DRIE with TEOS & PR mask for silicon cavity

(c) Filling the cavity with glass via anodic bonding and subsequent annealing.

(d) Planarization of BSG over surface of silicon wafer and leveling using HF wet etch

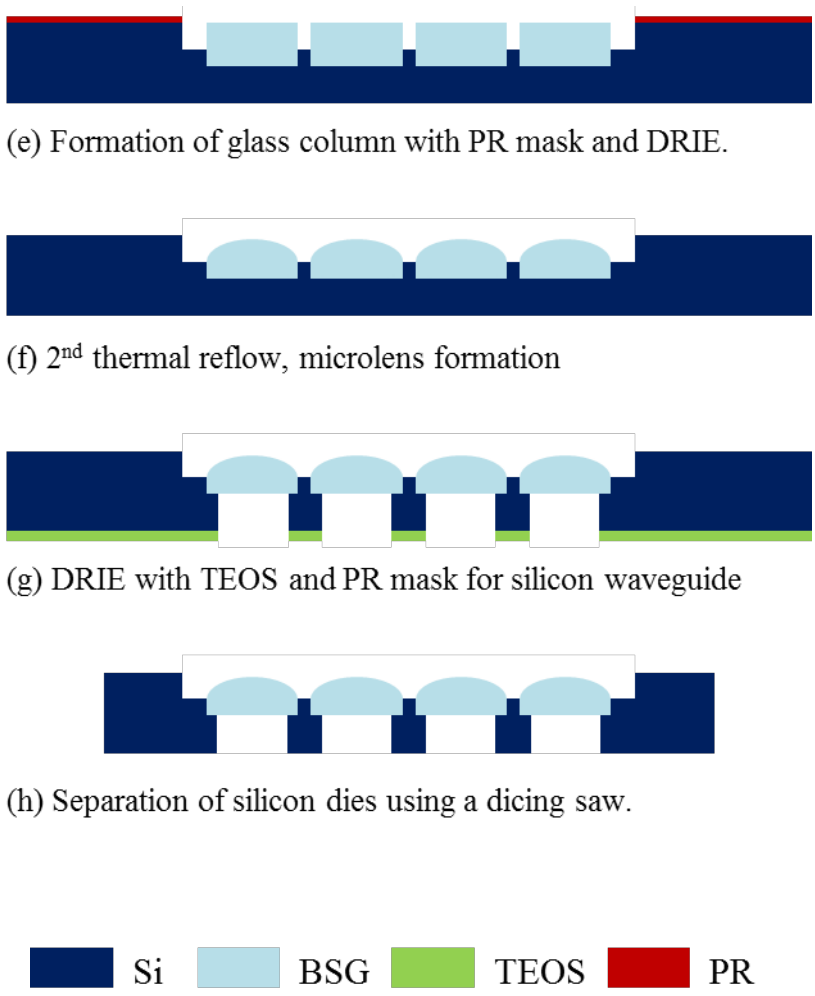

Figure 3.1 Schematic diagram of the fabrication process of the glass microlens array.

3.1.2 Fabrication results

The glass MLA (Figure 3.2 (a), (b)) has been monolithically integrated on 1 mm-thick, 5 mm x 5 mm silicon die, and it has been successfully fabricated by bulk-micromachining

processes. There are 4x4 microlens and 4x4 wave-guide holes on the silicon die for alignment of fibers which are directly inserted to holes with index matching epoxy (353ND, Epoxy Technology) applied to the tip of the fibers.

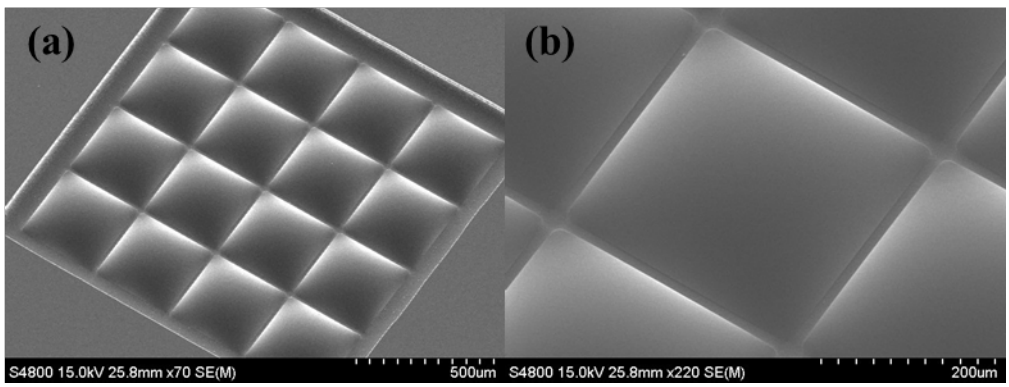

Figure 3.2 SEM image of (a) the monolithically fabricated MLA on a 5 mm x 5 mm silicon die, (b) magnified view of a single microlens.

Previously, the effectiveness of the glass microlens array has been verified experimentally, where a 3.13 dB enhancement of output light intensity has been achieved with a glass MLA compared to the output light intensity without the microlens array on the silicon die (Figure 3.3) [21].

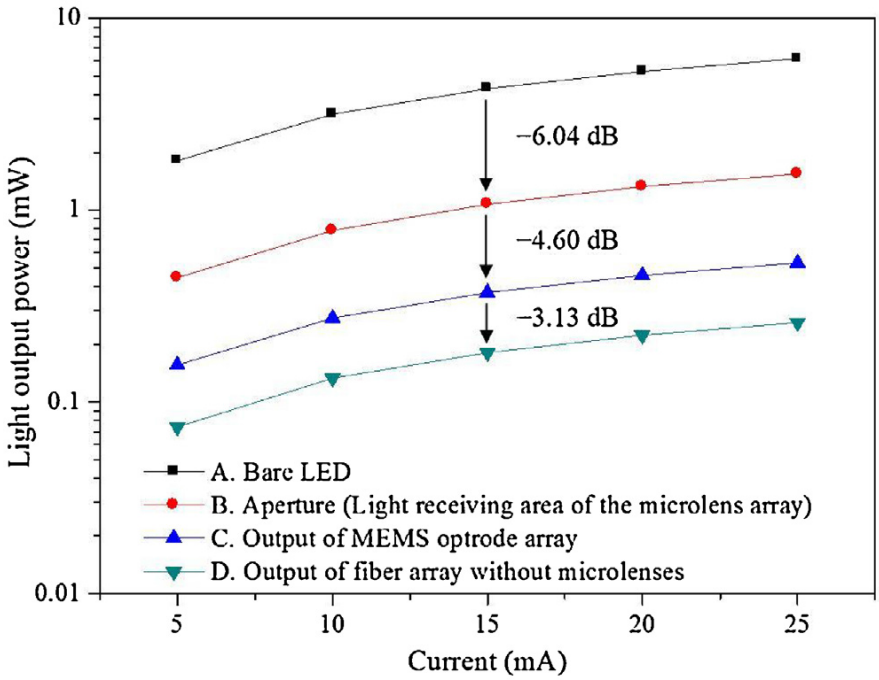

Figure 3.3 Comparison of the measured light output power between the samples A–D [21].

Furthermore, in some cases, there are failures of fabricated glass MLA by MEMS technology due to several reasons such as insufficient filling of cavity with BSG, overflowed BSG, and cracking in the silicon rim surrounding the lens (Figure 3.4). Also, crystallization on borosilicate glass during the high temperature annealing was one of main reasons of failures of fabrication of glass MLA. Surface crystallization is basically a nucleation of the cristobalite which is a high-temperature polymorph of silica on the glass surface. The cristobalite has the same chemical formula with SiO_2, but has a distinct crystal structure, thus has different physical and chemical characteristics compared to normal BSG. Increasing surface roughness and micro cracks on the surface cause change in refractive

index and a significant decrease in transmittance of BSG. To suppress the crystallizations on the BSG surface during the high temperature annealing process for thermal reflow, pre-treatment of plasma on the BSG surface before the annealing process for more than 100 seconds was suggested and verified [22]. After pre-treatment of plasma on the BSG surface, the number of cristobalites per unit area have been decreased to almost zero, and by doing so, the glass MLA have been fabricated successfully.

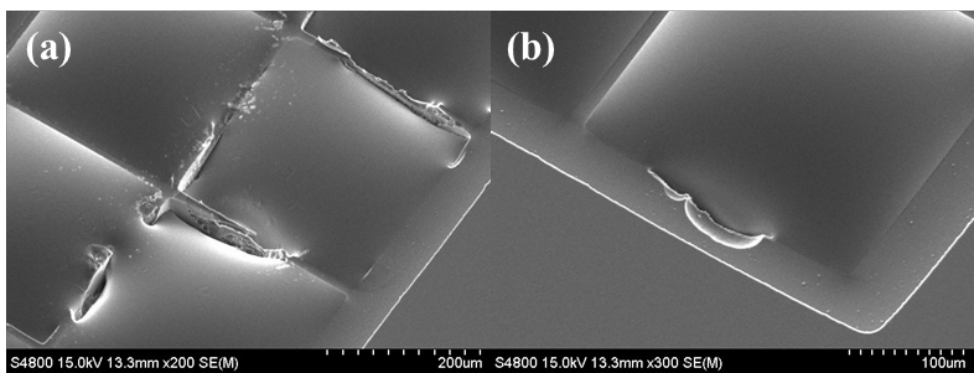

Figure 3.4 SEM images of failed to fabricate glass MLA due to (a) insufficient filling of cavity and overflowed BSG, (b) cracking in the silicon rim surrounding the lens.

3.2 Assembly

The glass MLA has been monolithically fabricated on a 1 mm-thick silicon substrate, and optical fibers have been assembled passively through the holes formed under the MLA. To fabricate the glass MLA assembled with optical fibers, the MLA and 16 optical fibers should be manually assembled (Figure 3.4). Thus, for alignment between holes and optical fibers, auxiliary devices are needed.

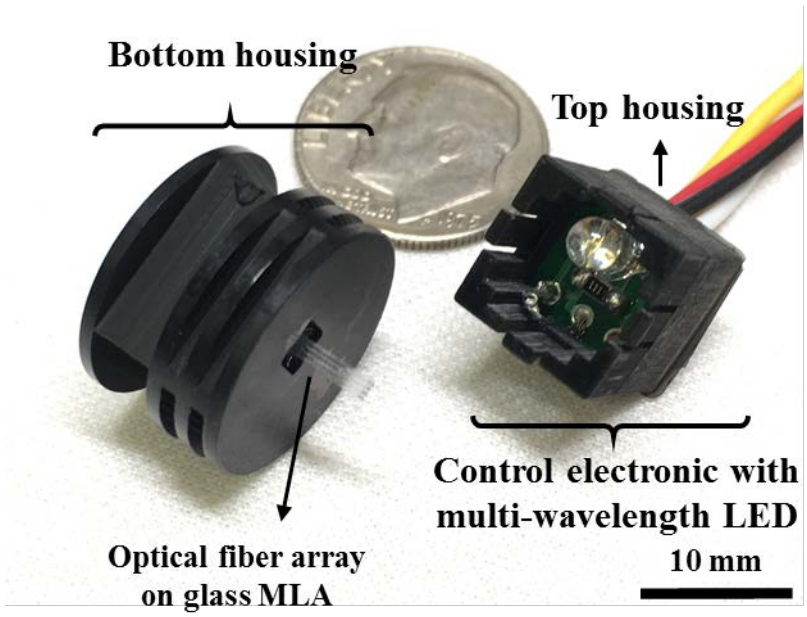

Figure 3.5 Optical image of a fully fabricated device with the assembled optical fibers on the glass MLA, control electronics with multi-wavelength LED, and top and bottom housing.

3.2.1 Optical fiber assembly

The high NA (NA= 0.5) optical fibers have been used for high coupling efficiency. The optical fibers are composed of pure silica core, hard polymer cladding, and tefzel coating. The tefzel coating are removed by a striping tool (T12S21, Thorlabs, Inc.). A high precision optical fiber cleaver (S326A, FITEL) with a ribbon fiber holder has been used for cutting fibers with uniform length and low surface roughness on both ends of optical fibers (Figure 3.5). The length of optical fibers are 6 mm. The ribbon fiber holder can be used to cut 12 optical fibers at a time, and the surface roughness of each fiber has an arithmetic average roughness, R_a of several tens of nanometers.

Figure 3.6 Optical image of the high precision fiber cleaver and ribbon holder.

A CNC (Computer Numerical Control)-milled aluminum jig which has two sockets on the top and bottom for fixing and aligning a silicon die with MLA, and a silicon die having the same size of a silicon die with MLA and 4x4 through-wafer-via (TWV) holes has been used to manually assemble 4x4 optical fibers and the silicon die with MLA. A brief description of the manual assembly procedure is as follows. First, after preparing all the components, the silicon die with MLA and silicon die with TWV are put in the bottom and top part of the aluminum jig, respectively. Next, after fixing the both silicon die inserted in the aluminum jig with tape, apply the index matching epoxy to the hole of MLA's holes and its surroundings for increasing light delivery efficiency and decreasing light loss on the interface between MLA and optical fibers. And then, by using a fiber tip tweezer, the optical fibers are inserted in the holes of silicon die with MLA in order. For straightness and alignment of the optical fibers, two silicon dies should be horizontal on the same y-axis and parallelize. Finally, after putting in the oven at 80 °C for 60 minutes, leave assembled silicon die for 30 minutes at room temperature for the curing process. Finally, the assembled silicon die with 4x4 MLA and 4x4 optical fibers are taken out from the aluminum jig. Figure 3.6 shows successfully assembled silicon die with MLA monolithically aligned optical fibers.

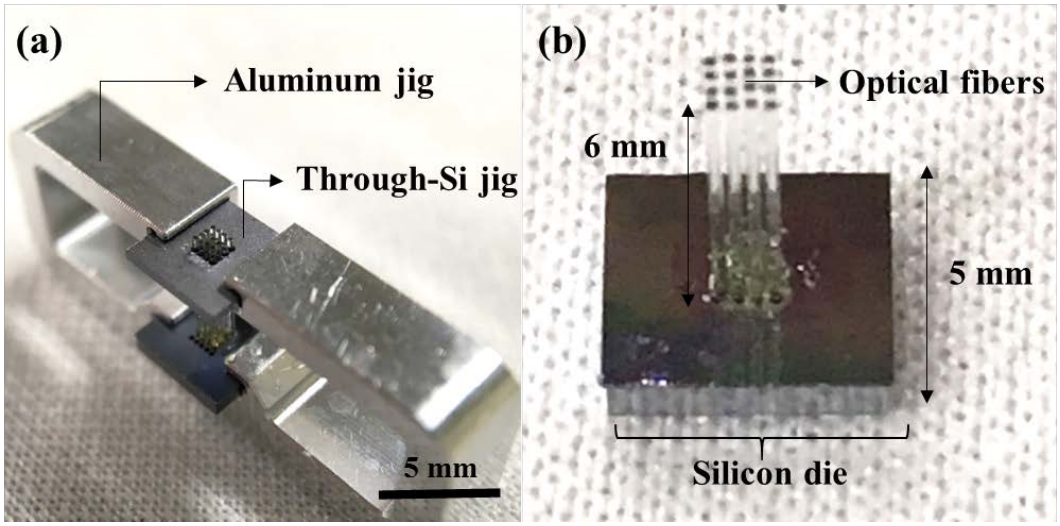

Figure 3.7 Optical images of (a) aligned optical fibers with aluminum jig and silicon die with 4x4 through-wafer-via (TWV) holes and (b) silicon die with assembled optical fibers.

3.2.2 Housing assembly

The sturdy housing is indispensable for fixing the device on the skull of the brain and protect the fragile components of the device. Figure 3.7 (a) shows successfully fabricated top and bottom parts of the device by using 3D printer with ABS-like resin. Figure 3.7 (b) shows the fully assembled device with top and bottom housing, control electronics, and silicon die with MLA and optical fibers. Due to the latch structure on both parts, it is easily disconnected and assembled, also the device is fixed well without additional fixation.

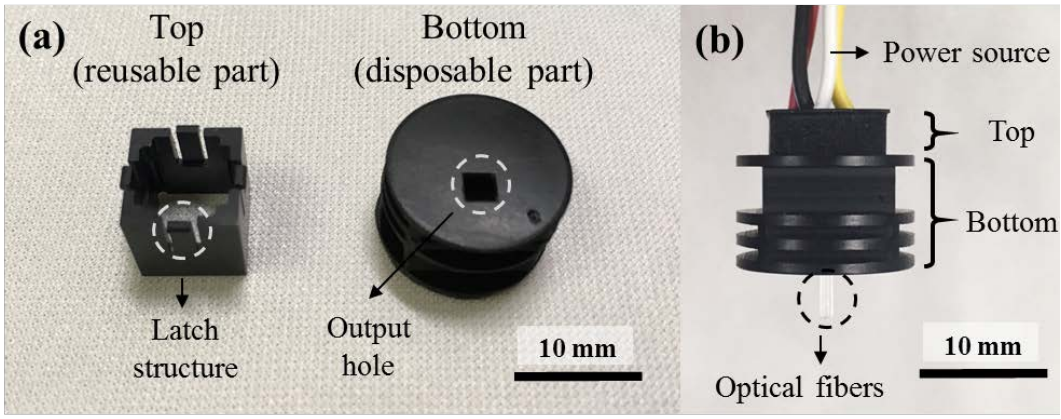

Figure 3.8 Optical images of (a) successfully fabricated top and bottom housing parts for the device, and (b) a fully assembled device. .

Chapter 4

Experiments

4.1 Measurement of light intensity

To verify the effectiveness of the fabricated device, several experiments have been conducted such as measurement of the light intensity, measurement of the heat dissipation, measurement of the spatial light distribution, and an animal *in vivo* test.

First of all, measurement of the light intensity has been conducted with a fully assembled device to verify the optical properties of this device. Figure 4.1 (a), (b) shows the blue (470 nm) and yellow (590 nm) light illumination of the operating device at 20 mA DC forward current. The light from the multi-wavelength LED is delivered through the MLA and optical fibers to the 4x4 fibers tip end.

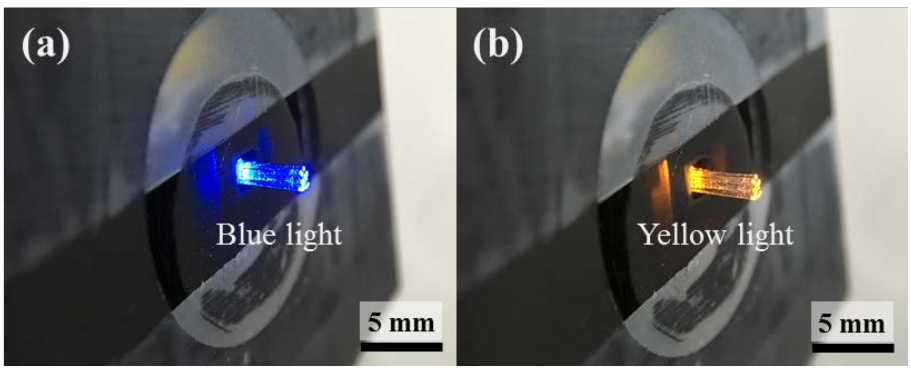

Figure 4.1 Optical images of light illumination of a fully assembled device at DC forward current , 20 mA: (a) blue, (b) yellow

4.1.1 Experimental setup

Figure 4.2 shows the schematic diagram of experimental setup for measurement of light intensity . It includes optical power meter (PM100D, Thorlabs, Inc.), photodiode power sensor (S121C, Thorlabs, Inc.), digital oscilloscope (TDS 2012, Tektronix), power supply (E3647A, Agilent), function generator (33120A, Agilent), and x, y, z micro manipulator. All the components have been set on the optical table which features excellent vibration isolation and optimized damping. A 4-DOF (degree-of-freedom) manual micro-manipulator has been used to adjust the alignment between PD power sensor and optical fiber tip and obtain maximum value of light power. The fully assembled device has been mounted on the head of the micro-manipulator which can regulate the distance of fiber tip and PD sensor in micro-scale.

As shown in Table 4.1, the experiment conditions for measurement of light intensity are summarized. All the experiments for measurement of light intensity have been conducted under the bright ambient light condition which can be slightly affect to the measured light intensity. The input current has been increased by 10 mA from 10 to 80 mA to measure the light power, and then the light power has been divided by the total cross-sectional area of 4x4 optical fiber tip which is 0.5027 mm^2 to obtain the light intensity. The blue and yellow light illumination has been tested and measured the light power at the same position.

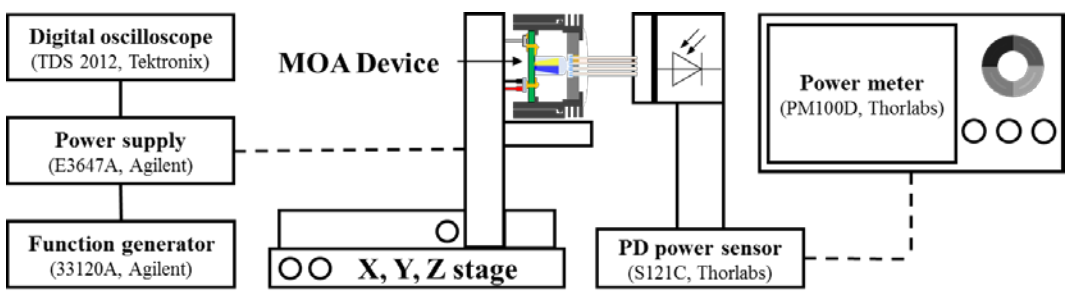

Figure 4.2 Schematic diagram of an experiment setup for measurement of light intensity.

Table 4.1 Experiment conditions for measurement of light intensity.

	Value	**Unit**
Input value	Current (10 ~ 80)	mA
Output value	Light power	mW
Wavelength	470, 590	nm
Ambient light condition	Bright	-

4.1.2 Results and discussion

Figure 4.3 shows the curve of measured light intensity when the input current increases by 10 mA from 10 to 80 mA. The experiment has been conducted continuously without turning off the LED when the experiment proceeds. The maximum light intensity under the suggested conditions has been obtained 3.35 mW/mm^2 at a dominant wavelength of 469 nm and 0.29 mW/mm^2 at a dominant wavelength of 590 nm when the input current was 80 mA. It could be expected that much higher light intensity would be achieved when the input LED current is over 80 mA, but the recommended input current for the LED should be under 100 mA. The measured light intensity has been increased linearly when the input current to the device has been increased.

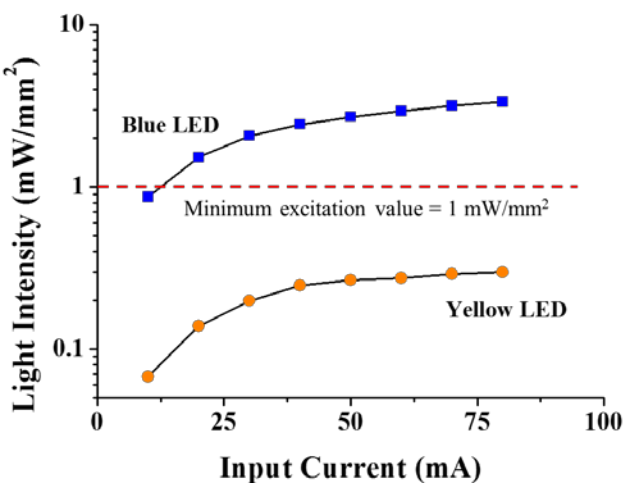

Figure 4.3 Measurement of the light intensity of the fully assembled device: the measured output light intensity on the fiber tip.

In terms of the light intensity, the measured light intensity has large differences between blue and yellow light despite the same input current to the device. To verify the different light intensity between blue and yellow light, two concepts of measuring spatial properties of light have been considered which are radiometry and photometry. In simple concept, the radiometry is the field of metrology dealing with the physical measurement of the properties of electromagnetic radiation across the total spectrum, including ultraviolet, visible and infrared light, and the photometry is subfield of radiometry; in other word, it illustrates the effects of visible light to the spectral response of the human eye by scaling the radiometric power in terms of brightness and color. Table 4.2 shows the common radiometric and photometric quantities. The radiometric quantities are simply related in energetic terms and the photometric quantities are related in visual terms. To compare the differences of light intensity of blue and yellow light at the same input current, the photometric value should be converted to radiometric value at the same input. Table 4.3 presents the optical characteristic of the multi-wavelength LED which is used in the device, and the actual luminous intensity of blue and yellow light at 20 mA has been measured from KOPTI (Korea Photonics Technology Institute) in South Korea by using source meter (2440, Keithley), spectrometer (SAS140CT, instrument system), and 0.5 m integrating sphere (ISP-500, KIMSOPTEC). The LED was placed at the center of the 0.5 m integrating sphere, and measured the luminous intensity of the LED using a source meter.

Table 4.2 Common radiometric and photometric quantities. (e: energetic, v: visual)

Radiometric			Photometric		
Quantity	**Symbol**	**Units**	**Quantity**	**Symbol**	**Units**
Radiant Power	Φ_e	W	**Luminous Flux**	Φ_v	lm (lumens)
Radiant Intensity	I_e	W/sr	**Luminous Intensity**	I_v	lm/sr, cd
Irradiance	E_e	W/m^2	**Illuminance**	E_v	lm/m^2
Radiance	L_e	$W/m^2 \cdot sr$	**Luminance**	L_v	$lm/m^2 \cdot sr$

Table 4.3 Optical characteristic of multi-wavelength LED (N500TBY4D, LigCom LED Group)

Dominant Wavelength (nm)	Luminous Intensity (20mA, mcd)	Measured Radiant Power (mW)	Viewing Angle (°)	Luminous efficiency function, $v(\lambda)$
468.3	**Actual value**	22.56	30	0.0974
	1783			
586.9	**Actual value**	2.04	30	0.8160
	1351			

The equation 4.1 shows that all the photometric quantities can be calculated from its radiometric equivalent and vice versa.

$$x_v = K_m \int xv(\lambda) d\lambda \tag{4.1}$$

where x_v is a photometric quantity, x is a corresponding radiometric quantity, v (λ) is the luminous efficiency function, K_m is the luminous efficacy (683 lm/W, at a wavelength of 555 nm) which is the scale factor carrying the proper value and units for v (λ). If the light source LED emits all of its light at the dominant wavelength, then the equation 4.1 can be simple algebraic conversion equation 4.2 to convert photometric unit to radiometric unit from which is Monochromatic conversion.

$$x_v = K_m x v(\lambda) \tag{4.2}$$

In table 4.3 the luminous efficiency function, v (λ) is obtained from an equation 4.3 at each dominant wavelength. The calculated luminous efficiency function's values are 0.0974 at a dominant wavelength of 468.3 nm and 0.8160 at a dominant wavelength of 586.9 nm when the applied input current was same.

$$v(\lambda) = 1.019e^{-285.4(\lambda-0.559)^2} \tag{4.3}$$

To obtain the radiometric quantity from the measured photometric quantity, the equation 4.2 can be converted to equation 4.4.

$$I_{e,\ blue} = \frac{I_v}{K_m v(\lambda{=}468.3\ [\mathrm{nm}])}, I_{e,\ yellow} = \frac{I_v}{K_m v(\lambda{=}586.9\ [\mathrm{nm}])} \quad (4.4)$$

The calculated radiometric unit, I_e of blue and yellow light at 20 mA (DC) was 0.0268 W/sr at a dominant wavelength of 468.3 nm and 0.0028 W/sr at a dominant wavelength of 586.9 nm. In this regard, there are 11.1 times difference between blue and yellow light, although it has a same input current and similar photometric quantity which is the luminous intensity. This differences are almost same with actually measured light intensity values of blue and yellow light which is 10.36 dB, which is 10.87 times difference. Thus, to obtain the same light intensity values of both blue and yellow light, the yellow should be applied much higher input current.

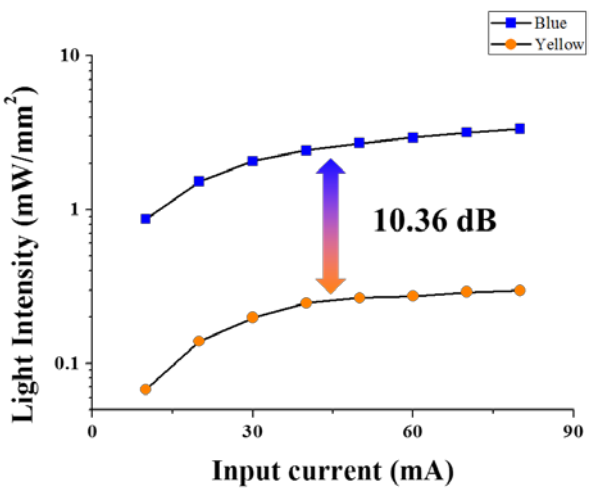

Figure 4.4 Average difference of measured light intensity of the fully assembled device.

Furthermore, the blue and yellow light have the light coupling efficiency of 4.91 % and 4.99 %, respectively. Fully assembled device has been maintained its stability and durability during the operation for measuring of light intensity, and it has been verified that there was little fluctuation of measured light intensity during the experiment. Also, Both the light intensity and the coupling efficiency can be improved by further optimization of individual parts, assembly processes, and overall system design.

4.2 Measurement of heat dissipation

To verify the effectiveness of the configuration that the device has enough long distance between a light source and optical fiber tip which is directly contacted with brain tissue, the measurement of heat dissipation experiment has been conducted by using a thermal imaging camera (A8303sc, FLIR) with a 4 x lens that has a spatial resolution of 3.5 μm in a controlled room which has stable temperature range and pneumatic flow.

4.2.1 Experimental setup

The thermal characteristic of a fully assembled device has been verified with measurement of heat dissipation of the optical fiber tips. Figure 4.5 shows the schematic diagram of experiment setup for measurement of heat dissipation. All experiments have been

conducted in the controlled room for excluding the effects from surrounding environment, thus temperature, humidity, air flow, and light illumination have been controlled. Each case of experiment has been proceeded after returning to the initial temperature which is the ambient temperature, after the previous experiment. A horizontal holder has been used for holding the fully assembled device during the test, and then, the thermal image camera has been installed on the same axis and the temperature change of optical fiber tips have been measured while moving along the x and y axes, and all successive recordings have been automatically stored at a connected computer. After that, the stored data can be analyzed the temperature characteristics at the desired position on the optical fiber tips using image analysis software program (FLIR Tools , FLIR® Systems, Inc.), and can extract continuous data over time with a graph and an Excel file. In table 4.2, there are three different cases for opsin stimulation which have different variables such as frequency, pulse width, current amplitude, and applying time for a specific target of opsin [23-25]. The input current of 30 mA has been applied for all cases to maintain the same light intensity which is 2.07 mW/mm^2 for blue illumination and 0.20 mW/mm^2 for yellow illumination.

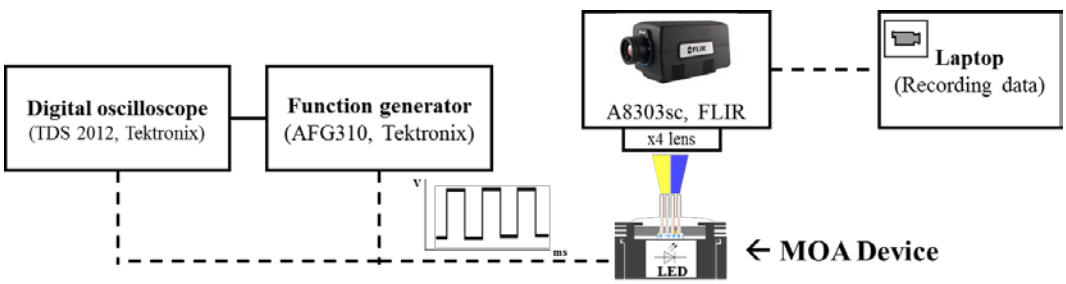

Figure 4.5 Schematic diagram of experiment setup for measurement of heat dissipation.

Table 4.2 Conditions for the stimulation of target opsin used in the thermal analysis.

Case	Frequency (Hz)	Pulse (ms)	Applying Time (s)	Target	Reference
1	20	1	30	ChR2	[23]
2	20	10	30	ChR2	[24]
3	10	50	0.5	ChETA	[25]

4.2.2 Results and discussion

The limitation of temperature rise of the implantable devices which are applicable for brain application is 0.5 °C due to thermal induced drawbacks such as deformation of molecular structure, and tissue damage that can lead to significant physiological and behavioral effects [20, 26, 27]. Thus, it is essential to maintain the thermally damaged tissue at a minimum to impede the vulnerable and sensitive brain tissue from damage. Figure 4.6 shows the measured heat variation on the fiber tips of case 1, 2 (in Table 4.2) for blue light. Figure 4.7 shows the measured heat variation on the fiber tips of case 1, 2 (in Table 4.2) for yellow light and Figure 4.8 shows the measured heat variation on the fiber tips of case 3 (in Table 4.2) for blue light. Also, Figure 4.9 shows the measured heat variation on the fiber tips of case 3 (in Table 4.2) for yellow light. Table 4.3 summarize the measured heat dissipation during the operation of the device at given conditions for blue and yellow light illumination. As shown in all the experiments data, the measured incline in temperature was lower than the limitation of temperature rise of 0.5 °C, and satisfied with preordained limitation. Thus, the developed device can be used for application in optogenetics.

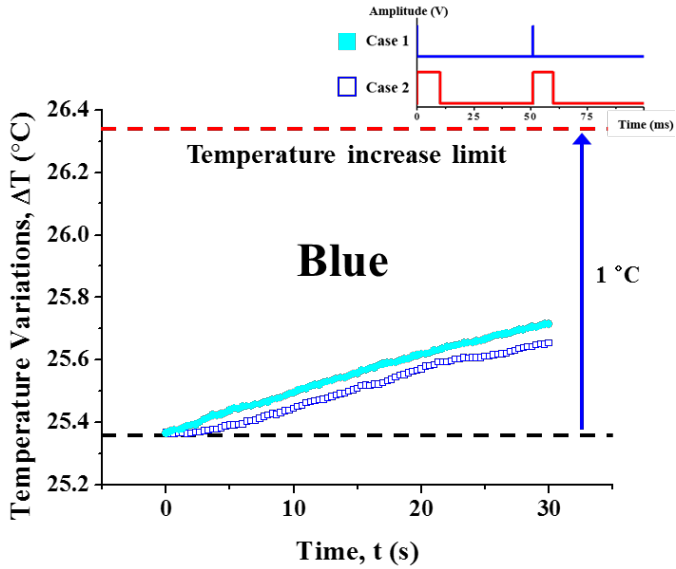

Figure 4.6 Measurement of the heat dissipation of the fully assembled device: measured heat variation on the fiber tip (Blue, case 1, 2).

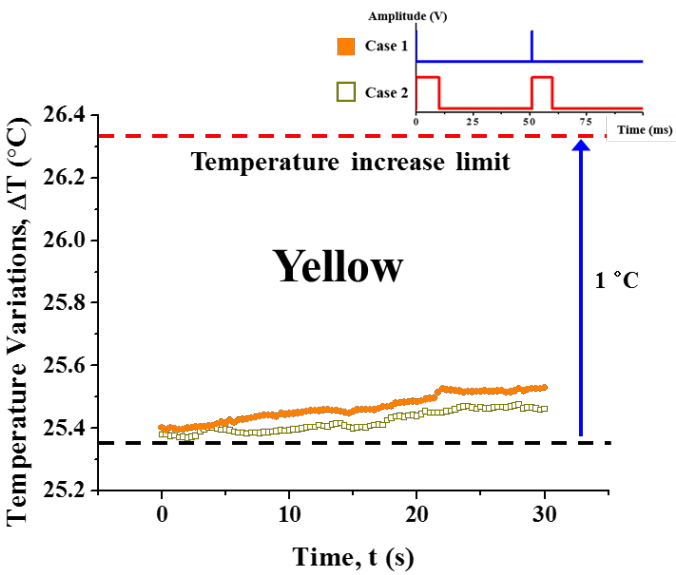

Figure 4.7 Measurement of the heat dissipation of the fully assembled device: measured heat variation on the fiber tip (Yellow, case 1, 2).

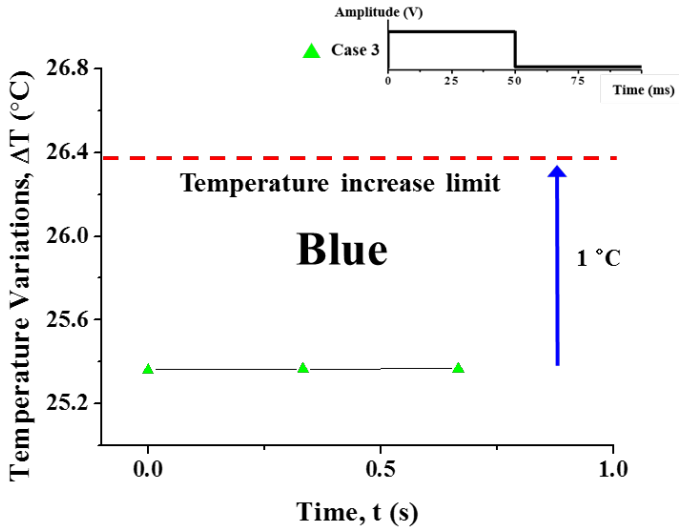

Figure 4.8 Measurement of the heat dissipation of the fully assembled device: measured heat variation on the fiber tip (Blue, case 3).

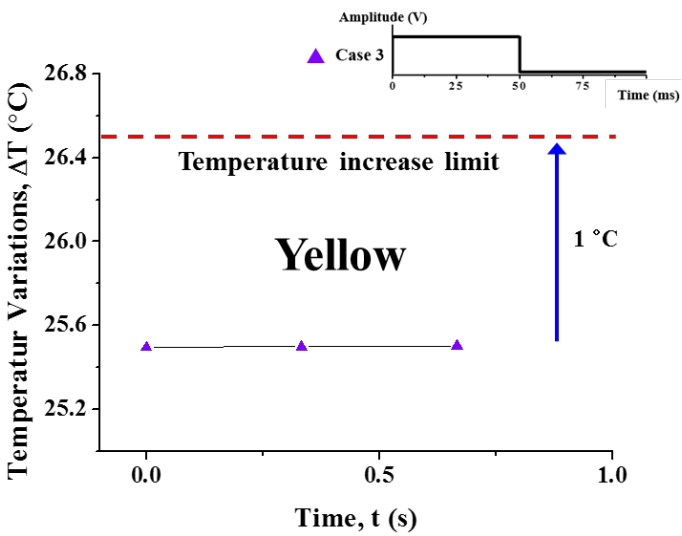

Figure 4.9 Measurement of the heat dissipation of the fully assembled device: measured heat variation on the fiber tip (Yellow, case 3).

Table 4.3 Summary of temperature rise at the optical fiber tips at given conditions.

Case	Blue light (℃)	Yellow light (℃)
Case 1	0.287	0.082
Case 2	0.349	0.128
Case 3	0.001	0.007

In case of case 3, the operating time is 0.5 s, thus the results of temperature rise could be not reliable to deduce that the experimental results would show the same results every time the experiment is repeated. However, the results are sound, because the temperature rise is unperceivable and sufficiently lower than the limitation of temperature rise of 0.5 °C.

Moreover, Although not provided in this paper, both scattering and absorbance vary with light wavelengths, with absorbance ~10 times higher at 475 nm than 600 nm [28]. Thus, despite under the same conditions of light intensity with different wavelength light source delivering to the brain through the same optical waveguide, the result of temperature rising would be markedly different for different wavelengths.

4.3 Measurement of the spatial light distribution

The spatial light distribution at the optical fiber tips has been measured to characterize the virtual light distribution of the developed device when it is inserted into the brain-like material which is 0.6 % agarose gel . Agarose gel at a 0.6 % concentration closely resembles *in vivo* brain with respect to several critical physical characteristics such as the ratio of

distribution volume to infusion volume, the infusion pressure, Gadodiamide infusion, and the force profile for insertion of a silastic catheter, thus agarose gel (0.6 %) is a useful surrogate for *in vivo* brain in exploratory studies [29]. In this regard, the insertion of developed device to 0.6 % agarose gel would simulate the actual spatial light distribution.

4.3.1 Experimental setup

Figure 4.10 shows the schematic diagram of experiment setup for measurement of spatial light distribution. A x, y, z manipulation holder has been used to fix the developed device, and the optical fiber tips which are installed at the bottom part of the disposable part have been carefully inserted into 0.6 % agarose gel. The optical fiber tips have been located at 5 mm under the surface of agarose gel. The input current was 20 mA (DC), which can be converted to the light intensity of 1.52 mW/mm^2 and 0.16 mW/mm^2 for blue and yellow light, respectively. In table 4.4, the experiment conditions are summarized.

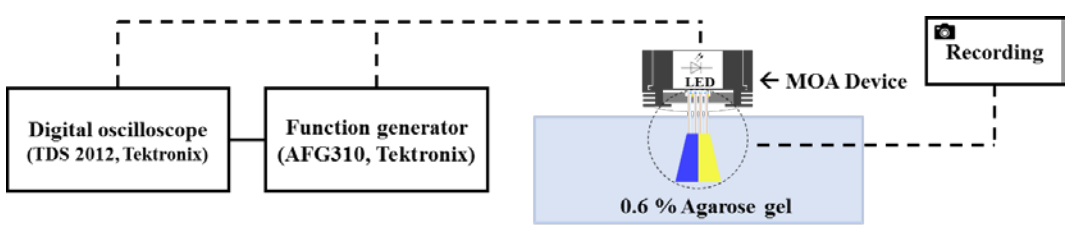

Figure 4.10 Schematic diagram of experiment setup for measurement of spatial light distribution.

Table 4.4 Experiment conditions for measurement of spatial light distribution.

	Value	Unit
Material	0.6 % Agarose gel	-
Input current (DC)	20	mW
Light intensity	1.52 (Blue)	mW/mm^2
	0.16 (Yellow)	mW/mm^2

4.3.2 Results and discussion

Figure 4.11 (left) is a captured optical image of developed device which is inserted into 0.6 % agarose gel while the device continuously illuminates blue light to the downward. The figure 4.11 (right) shows the relative light intensity of the blue light extracted from the captured image by using image analysis processing with an engineering software (MATLAB, The MathWorks, Inc.). The extracted image represents the distribution of normalized relative light intensity according to actual brightness of the blue light and it is possible to confirm the relative light intensity according to the depth from the end of the fiber tips to the downward direction. As the distance from the tip end to the downward direction increases, the relative light intensity has been decreased and also, the light spectra has been spread widely. The relative light intensity of the blue light has been maintained approximately 91 % of the maximum value until 2 mm-length from the end of the optical fiber tips. In figure 4.12, the relative intensity of blue light with distance from the fiber tip has been shown. Figure 4.13 represents measured FWHM (Full Width at Half Maximum)

which as the distance increases from the tips, the light has been spread to a wider range, and at 2 mm from the tip the measured FWHM is 0.087 which is normalized distance from the captured image.

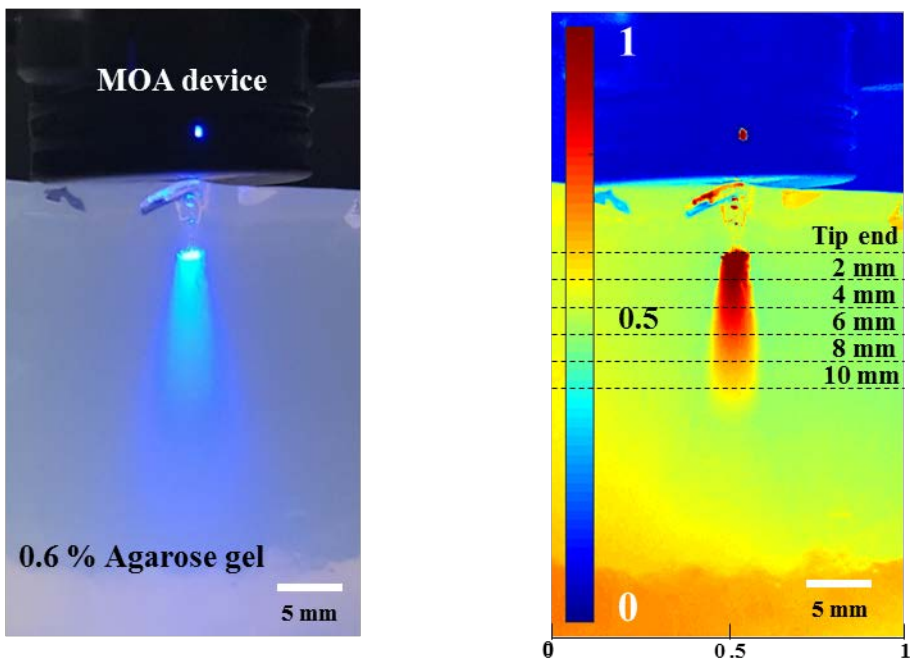

Figure 4.11 Optical images of (left) blue (470 nm) light illumination of the developed device inserted into 0.6 % agarose gel and (right) relative intensity of the blue (470 nm) light extracted from the captured image.

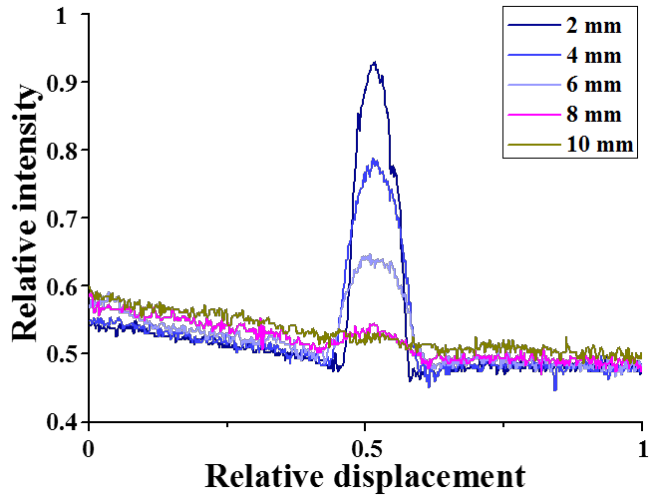

Figure 4.12 Measured light spatial distribution of the developed device inserted into 0.6 % agarose gel (Blue): Relative intensity with distance from the fiber tip

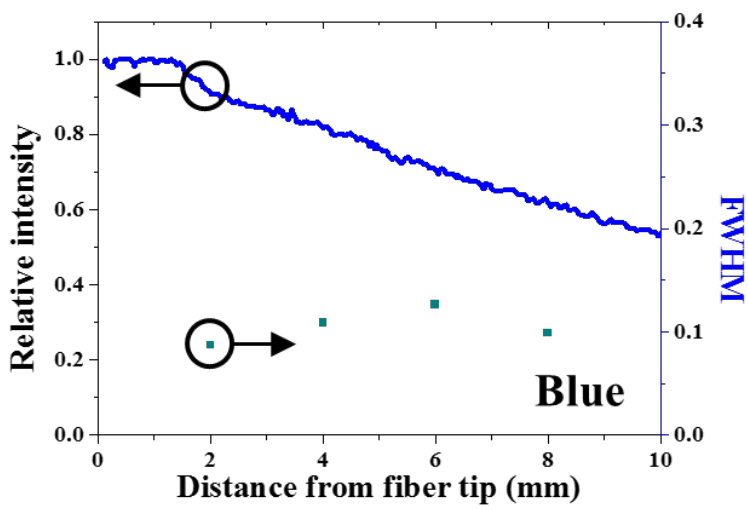

Figure 4.13 Measured light spatial distribution of the developed device inserted into 0.6 % agarose gel (Blue): Relative intensity and FWHM variations as distance increases from the optical fiber tip.

As shown in Figure 4.14, the relative light intensity of the yellow light extracted from the captured image. All the experiments conditions were same as blue cases, and the relative light intensity of the yellow light has been maintained approximately 98 % of maximum value until 2 mm-length from the end of the optical fiber tips. In figure 4.15, the relative intensity of yellow light with distance from the fiber tips has been shown. Also, the obtained FWHM at 2 mm from the tips is 0.115 for the yellow light (Figure 4.16).

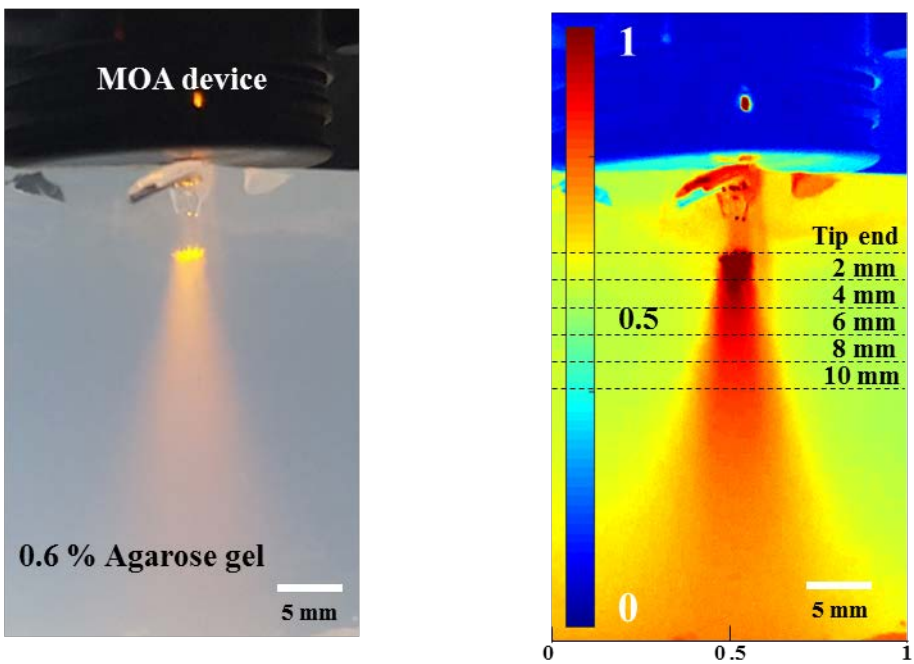

Figure 4.14 Optical images of (left) yellow (590 nm) light illumination of the developed device inserted into 0.6 % agarose gel and (right) relative intensity of the yellow (590 nm) light extracted from the captured image.

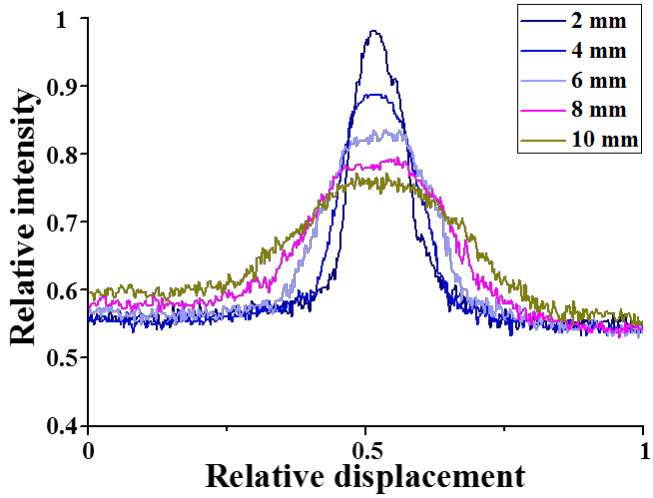

Figure 4.15 Measured light spatial distribution of the developed device inserted into 0.6 % agarose gel (Yellow): Relative intensity with distance from the fiber tip

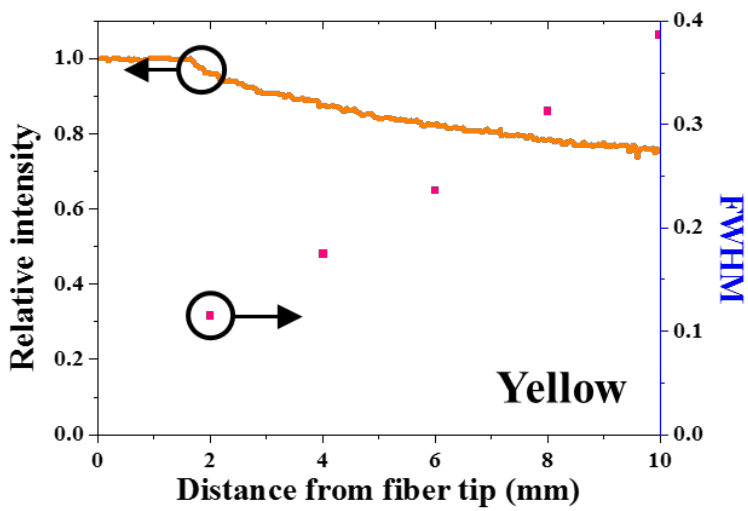

Figure 4.16 Measured light spatial distribution of the developed device inserted into 0.6 % agarose gel (Yellow): Relative intensity and FWHM variations as distance increases from the optical fiber tip.

In terms of FWHM, the spatial light distribution of blue and yellow has a little different tendency which the blue light reaches a maximum value near 6 mm-length from the optical fiber tip, whereas the yellow light penetrates into the agarose gel and shows linearly increasing tendency. Although it is well known that the longer the wavelength, the deeper the depth of penetration of the light, it deserves to figure out the difference of penetration trends with the blue and yellow light for the advancement of the field of optogenetics.

4.4 Animal *in vivo* test

To verify the feasibility of the developed LED-based optical neural implants for optogenetics, the *in vivo* animal experiments have been conducted. The disposable part of the device has been mounted on top of the primary visual cortex of a transgenic mouse which is expressing ChR2 under the promotor of CaMKIIα [30].

4.4.1 Measurement of spiking activities of excitatory neurons

A Michigan type silicon multichannel neural probe (A1x32-Poly2, Neuronexus) has been inserted into the primary visual cortex and used for recording the neural spiking activity of excitatory neurons. The measured blue (a dominant wavelength: 470 nm) light power of the device at the tip of the optical fiber array was 0.22 mW and a single continuous light pulse was provided for 1 sec. The measurement of neural activity have been carried out in

three sections which are before, during, and after the light illumination each for 1 sec, and total 160 multi-units from the mouse were measured. During turn on the light, the measured neural activity was more than twice as much as before turn on the light.

4.4.2 Modification of perceptive behavior of a mouse

The modification of perceptual behavior of the mouse has been tested with developed LED-based optical neural implant. The implant has been chronically inserted into the primary visual cortex of the transgenic mouse and stimulated the target area to control and modify behavior of the mouse [31]. The experiment was conducted under the conditions that the light power was 0.22 mW, the frequency of the light was 10 Hz, and the duration was 0.5 sec. The blue light, which is a cue sign for the water reward, was delivered through the 4x4 optical fiber array, and it stimulate the visual cortex of the mouse in the dark chamber. The training of the mouse with the blue light illumination was carried out for consecutive 9 days. When the mouse licks the water port with the blue light illumination (LED on), the mouse gets water as a reward and the action is counted as a hit, on the other hand, the mouse does not lick while the LED is on, the action is counted as a miss. If the mouse licks the port under LED off condition, the mouse is punished slightly with an air puff and a timeout delay, and the action is counted as a false alarm. If the mouse does not lick, the action is counted as a correct rejection. Earlier in the experiment, the expected results were: if the LED blue light illumination can properly stimulate the cortical neurons in the visual

cortex, the mouse would learn the training and show increased hit rates and decreased false alarm rates. The correct rejection rate on the first day of training was 49 % and it was improved to 83 % on the 9^{th} days of training.

Consequently, the developed LED-based optical neural implant can effectively deliver the light to the target area and can sufficiently drive cortical neurons by generating the perceptual experience in behaving animals.

Chapter 5

Conclusion

In this research, a new type of multi-wavelength LED-based optical neural implant for excitation and inhibition of target cells has proposed. The developed device ultimately will be adapted to fully wireless system for freely behaving animal optogenetic experiments. The device has been successfully fabricated. Through monolithically fabricated microlens array and high NA optical fiber array, the high coupling efficiency has been achieved. The feasibility of the multi-wavelength illumination system by using a single conventional LED, scalability of the aligned optical fiber array, and ability to stimulate of multiple target area have been verified. Possibility of brain damage due to light induced temperature rising has been minimized by physical separation of the light source and facets of optical fiber tip. *In*

vivo experiment with the developed device on a transgenic mouse has proved that this device can successfully deliver specific light from the light source, and properly stimulate the target area. Moreover, this device can utilize for training of perceptual behaviors in the mouse by stimulating target neurons.

Bibliography

[1] P. Rajasethupathy, E. Ferenczi, and K. Deisseroth, "Targeting Neural Circuits," *Cell*, vol. 165, no. 3, pp. 524-534, 2016.

[2] F. Crick, "The impact of molecular biology on neuroscience," *Philosophical transactions of the Royal Society of London. Series B, Biological sciences*, vol. 354, no. 1392, pp. 2021-2025, 1999.

[3] E. S. Boyden, F. Zhang, E. Bamberg, G. Nagel, and K. Deisseroth, "Millisecond-timescale, genetically targeted optical control of neural activity," *Nat Neurosci*, vol. 8, no. 9, pp. 1263-8, Sep 2005.

[4] K. Deisseroth, "Optogenetics," *Nat Methods*, vol. 8, no. 1, pp. 26-9, Jan 2011.

[5] R. P. Kale, A. Z. Kouzani, K. Walder, M. Berk, and S. J. Tye, "Evolution of optogenetic microdevices," (in eng), *Neurophotonics*, vol. 2, no. 3, p. 031206, Jul 2015.

[6] A. M. Aravanis *et al.*, "An optical neural interface: in vivo control of rodent motor cortex with integrated fiberoptic and optogenetic technology," *J Neural Eng*, vol. 4, no. 3, pp. S143-56, Sep 2007.

[7] E. Iseri and D. Kuzum, "Implantable optoelectronic probes for in vivo optogenetics," (in eng), *J Neural Eng*, vol. 14, no. 3, p. 031001, Jun 2017.

[8] B. Fan and W. Li, "Miniaturized optogenetic neural implants: a review," *Lab on a Chip*, 10.1039/C5LC00588D vol. 15, no. 19, pp. 3838-3855, 2015.

[9] Y. LeChasseur *et al.*, "A microprobe for parallel optical and electrical recordings from single neurons in vivo," (in eng), *Nat Methods*, vol. 8, no. 4, pp. 319-25, Apr 2011.

[10] P. Anikeeva *et al.*, "Optetrode: a multichannel readout for optogenetic control in freely moving mice," (in eng), *Nat Neurosci*, vol. 15, no. 1, pp. 163-70, Dec 4 2011.

[11] J. Wang *et al.*, "Integrated device for combined optical neuromodulation and electrical recording for chronic in vivo applications," (in eng), *J Neural Eng*, vol. 9, no. 1, p. 016001, Feb 2012.

[12] Y. Son *et al.*, "A new monolithically integrated multi-functional MEMS neural probe for optical stimulation and drug delivery," in *2015 28th IEEE International Conference on Micro Electro Mechanical Systems (MEMS)*, 2015, pp. 158-161.

[13] A. N. Zorzos, J. Scholvin, E. S. Boyden, and C. G. Fonstad, "Three-dimensional multiwaveguide probe array for light delivery to distributed brain circuits," *Optics Letters*, vol. 37, no. 23, pp. 4841-4843, 2012/12/01 2012.

[14] N. Grossman *et al.*, "Multi-site optical excitation using ChR2 and micro-LED array," (in eng), *J Neural Eng*, vol. 7, no. 1, p. 16004, Feb 2010.

[15] K. Y. Kwon, B. Sirowatka, A. Weber, and W. Li, "Opto- muECoG array: a hybrid neural interface with transparent muECoG electrode array and integrated LEDs for optogenetics," (in eng), *IEEE Trans Biomed Circuits Syst*, vol. 7, no. 5, pp. 593-600, Oct 2013.

[16] M. Schwaerzle, P. Elmlinger, O. Paul, and P. Ruther, "Miniaturized 3×3 optical fiber array for optogenetics with integrated 460 nm light sources and flexible electrical interconnection," in *2015 28th IEEE International Conference on Micro Electro Mechanical Systems (MEMS)*, 2015, pp. 162-165.

[17] K. Y. Kwon, H. M. Lee, M. Ghovanloo, A. Weber, and W. Li, "Design, fabrication, and packaging of an integrated, wirelessly-powered optrode array for optogenetics application," (in eng), *Front Syst Neurosci*, vol. 9, p. 69, 2015.

[18] N. McAlinden *et al.*, "Thermal and optical characterization of micro-LED probes for in vivo optogenetic neural stimulation," *Optics Letters*, vol. 38, no. 6, pp. 992-994, 2013/03/15 2013.

[19] T. I. Kim *et al.*, "Injectable, cellular-scale optoelectronics with applications for wireless optogenetics," (in eng), *Science*, vol. 340, no. 6129, pp. 211-6, Apr 12 2013.

[20] P. Andersen and E. I. Moser, "Brain temperature and hippocampal function," (in English), *Hippocampus*, vol. 5, no. 6, pp. 491-498, 1995.

[21] S. Yoo, H. Lee, S. B. Jun, Y.-K. Kim, and C.-H. Ji, "Disposable MEMS optrode array integrated with single LED for neurostimulation," *Sensors and Actuators A: Physical*, vol. 273, pp. 276-284, 2018.

[22] Y. Sunghyun, "Disposable MEMS optrode array for multi-wavelength

neurostimulation," Ph.D. dissertation, Seoul National University, Seoul, Republic of Korea, 2017.

[23] I. Diester *et al.*, "An optogenetic toolbox designed for primates," *Nat Neurosci,* vol. 14, no. 3, pp. 387-97, Mar 2011.

[24] E. B. Larson, A. M. Wissman, A. L. Loriaux, S. Kourrich, and D. W. Self, "Optogenetic stimulation of accumbens shell or shell projections to lateral hypothalamus produce differential effects on the motivation for cocaine," *J Neurosci,* vol. 35, no. 8, pp. 3537-43, Feb 25 2015.

[25] F. Yang *et al.*, "Light-controlled inhibition of malignant glioma by opsin gene transfer," *Cell Death Dis,* vol. 4, p. e893, Oct 31 2013.

[26] E. Moser, I. Mathiesen, and P. Andersen, "Association between brain temperature and dentate field potentials in exploring and swimming rats," *Science,* vol. 259, no. 5099, pp. 1324-1326, 1993.

[27] M. A. Long and M. S. Fee, "Using temperature to analyse temporal dynamics in the songbird motor pathway," *Nature,* Article vol. 456, p. 189, 11/13/online 2008.

[28] A. N. Yaroslavsky, P. C. Schulze, I. V. Yaroslavsky, R. Schober, F. Ulrich, and H. J. Schwarzmaier, "Optical properties of selected native and coagulated human brain tissues in vitro in the visible and near infrared spectral range," *Physics in Medicine & Biology,* vol. 47, no. 12, p. 2059, 2002.

[29] Z. J. Chen *et al.*, "A realistic brain tissue phantom for intraparenchymal infusion studies," (in eng), *J Neurosurg,* vol. 101, no. 2, pp. 314-22, Aug 2004.

[30] S. Jeon *et al.*, "Multi-wavelength light emitting diode-based disposable optrode array for in vivo optogenetic modulation," (in eng), *J Biophotonics,* p. e201800343, Dec 26 2018.

[31] Y. H. Song *et al.*, "A Neural Circuit for Auditory Dominance over Visual Perception," (in eng), *Neuron,* vol. 93, no. 5, pp. 1236-1237, Mar 8 2017.

국문 초록

본 연구에서는, 광 유전학 연구를 위한 새로운 형태의 다중 파장 발광 다이오드 (LED) 기반 광학 신경 인터페이스가 제안 되었다. 이 장치는 크게 재사용 가능한 부분과 일회용 부분으로 나뉘어 진다. 재사용 가능한 부분은 기존의 상용화된 다중 파장 발광 다이오드 (LED)가 결합된 전자 제어 장치로 구성되며, 일회용 부분은 초소형 정밀기계 기술을 이용하여, 제작과정에서 일체형으로 제작된 마이크로 렌즈 어레이와, 수동으로 결합된 광섬유 어레이가 배열 되어 있는 실리콘 시편으로 구성되어 있다. 두 부분 모두 3D 프린터를 이용해서 제작된 하우징에 결합 되어 있으며, 결합 부위에 걸쇠 구조를 가지고 있어 조립과 분리가 용이하도록 제작 되어있다. 측정된 빛강도는 인가 전류가 80 mA 일 때 469 nm 에서 3.35 mW/mm^2 이고, 590 nm 에서 0.29 mW/mm^2로 측정 되었다. 광원에서부터 열전달에 의한 광섬유 끝단의 온도 변화를 측정하였고, 모든 시험 조건에서 미국의 FDA 및 IEC 표준을 만족 하는 결과를 얻었다. 또한 광섬유 끝단으로부터 2 mm 거리까지 상대 광도의 약 90 % 이상이 유지되었다. 생체내 동물 실험에서 뉴런의 표면에 Channelrhodopsin-2를 나타내는 유전자 변이 생쥐의 신경활동을 측정하였고, 개발된 장치를 이용해서 대상 영역에 빛을 전사 하였다. 대상 영역의 뉴런 활동이 빛을 전사 하지 않았을 경우와 비교 하였을 때, 두 배 이상 증가하

였고, 또한 쥐의 행동 실험을 통해 제작된 장치가 대상 영역으로 성공적으로 빛을 전달하고, 충분하게 뉴런 활동을 자극할 수 있다는 것을 확인 하였다. 측정된 결과는 전달된 빛이 뇌의 피질 부위의 뉴런을 자극하고 쥐의 지각적인 부분에 영향을 미칠 수 있다는 것을 보여주었다. 결과적으로, 개발된 장치는 광유전학 연구에 적용 가능함을 확인 하였다.